ISME

Coupled Thermoelasticity Impact Response Analysis of Composite Plates with SMA Wires in Thermal Environments

A. Niknami[*]
Ph.D Candidate

M. Shariyat[†]
Professor

Impact responses of rectangular composite plates with embedded shape memory alloy (SMA) wires are investigated in the present research. The plate is assumed to be placed in a thermal environment; so that in contrast to the available researches in the field, the shape memory and ferroelasticity effects have to be considered also in addition to the superelasticity. The governing equations are derived based on a proposed enhanced free energy function and refined constitutive equations with coupled thermoelasticity expressions and solved by the finite element method. The resulting governing equations are solved through an iterative solution scheme, a bridging law, and a special phase transformation tracing algorithm. A special case of the results is verified by the experimental results extracted by the authors. Results showed that the volume change rate, impact-induced temperature rise, and ambient temperature may significantly affect the phase transformations mechanism and the non-linear indentation phenomenon.

Keywords: Coupled thermoelasticity impact analysis, Shape memory alloy, Pseudoelasticity, Ferroelasticity, Experimental results.

1 Introduction

Due to their remarkable weight savings, composite components have extensively been employed as alternatives to their metallic counterparts in the hi-tech structures. The composite structures may be prone to impacts. A portion of the undesired impact energy may be dissipated through using embedded shape memory elements [1, 2] that act solely based on the internal phase transformations of the microstructure of the material and do not rely upon the external energy supply.

Majority of the researches on low velocity impact of the SMA composite plates have been accomplished through using simplification assumptions. Shariyat et al. [3] and Shariyat and Moradi [4] through modifying Brinson's model to trace the local loading and unloading and reverse loading events, investigated forced vibration and impact responses of composite plates with embedded SMA wires, respectively.

[*]Ph.D Candidate, Faculty of Mechanical Engineering, K.N. Toosi University of Technology, Pardis Street, MolaSadra Avenue, Vanak Square, Tehran, Iran.
[†] Corresponding Author, Professor, Faculty of Mechanical Engineering, K.N. Toosi University of Technology, Pardis Street, MolaSadra Avenue, Vanak Square, Tehran, Iran, m_shariyat@yahoo.com

Recently, Shariyat and Hosseini [5] have extended these ideas through investigating eccentric impact of the preloaded SMA composite plates, proposing a mixed-order hyperbolic global-local plate theory.

Some researchers studied effects of the volume change rate in terms of the resulting temperature rise and phase transform process [6-11]. In general, the mechanical behavior and failure modes of the materials significantly depend on the velocity of the applied loads and consequently, the strain-rate that is generally coupled with the temperature rise.

In the present research, a comprehensive formulation is developed for impact analysis of composite plates with embedded shape memory alloys. The highly non-linear governing equations are derived based on orthogonal integral formulations and solved by an iterative solution procedure. Based on the presented brief literature survey, novelties of the present research may be summarized as:

1- Effects of the strain-rate on the phase transformation process are considered.
2- In contrast to the available researches, the shape memory and ferroelasticity effects of the SMA wires are also included in the analysis.
3- Proposing a revised general Helmholtz free energy and a revised Brinson's model for the SMAs to include some new parameters, such as the reverse loading and the latent heat of the phase transformation.
4- Proposing a refined contact law that is consistent with the foregoing items.
5- Relating mechanical properties of the SMA wires to those of the lamina through an adequate bridging law.
6- Solving the modified nonlinear constitutive equation by a return-mapping Newton-Raphson scheme, within each numerical time integration step.
7- Validating the results by the experimental results prepared by the authors.

2 The governing equations

2.1 Description of the geometry and the material properties

A schematic representation of the considered composite plate, the embedded shape memory alloy (SMA) wires, and the spherical indenter are shown in Figure (1). Length, width, and thickness of the plate are denoted by *a*, *b*, and *h*, respectively and initial velocity and radius of the spherical indenter are denoted by *V* and *R*, respectively.

According to Voigt and Reuss micro-mechanical homogenization techniques, effective material properties of the composite may be determined based on the volume fractions of the fiber and matrix [12], as follows:

$$E_1 = E_f V_f + E_m V_m \ , \quad E_2 = \frac{E_f E_m}{E_f V_m + E_m V_f} \ , \quad \nu_{12} = \nu_f V_f + \nu_m V_m \ , \quad G_{12} = \frac{G_f G_m}{G_f V_m + G_m V_f} \qquad (1)$$

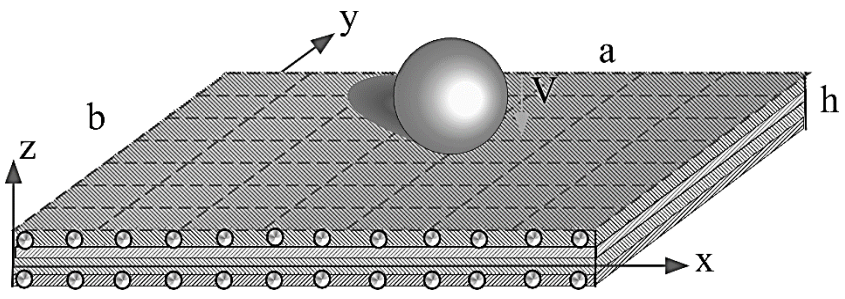

Figure 1 The considered composite plate with embedded shape memory alloy wires and the employed second-order rectangular elements.

where V_f and V_m are volume fractions of the fiber and matrix, respectively, and the *f* and *m* subscripts denote the fiber and matrix, respectively.

2.2 Development of the modified free energy function and the revised constitutive law of the SMA

The Clausius–Duhem inequality [13] may be written as follows for a reversible process:

$$q_{i,i} - \sigma_{ij}\dot{\varepsilon}_{ij} + \rho_0\left(\dot{\psi} + \dot{T}\eta\right) - \rho_0\left(r - T\dot{\eta}\right) = 0 \tag{2}$$

where, $\boldsymbol{q}$, σ_{ij}, ε_{ij}, ρ_0, ψ, T, η, and r are the heat flux vector, stress tensor, strain tensor, mass density, Helmholtz free energy, absolute temperature, entropy, and the internal heat generation, respectively. The comma symbol denotes a partial differentiation with respect to the indicated parameter. Some of the quantities may be defined in terms of the Helmholtz free energy:

$$\sigma_{ij} = \rho_0 \frac{\partial \psi}{\partial \varepsilon_{ij}}, \qquad \eta = -\frac{\partial \psi}{\partial T}, \qquad \Lambda = -\rho_0 \frac{\partial \psi}{\partial \xi} \tag{3}$$

where, Λ is the driving force of the transformation and ξ is the martensite volume fraction. For the SMA, the Helmholtz free energy is a function of the strain, temperature, and martensite volume fraction. By substituting Eq. (3) into Eq. (2), one has:

$$q_{i,i} - \Lambda\dot{\xi} - \rho_0\left(r - T\dot{\eta}\right) = 0 \tag{4}$$

As may be noted from Eq. (4), rate of the impact-induced martensite volume fraction affects the first law of thermodynamics and consequently, the energy balance equation. Comparing the relevant expression in Eq. (4) with the remaining terms reveals that this expression plays a heat generation role in the first law of thermodynamics. The free energy expression that accounts for the martensite phase transformations of the SMA material may be proposed as:

$$\begin{aligned}\psi = {} & \frac{1}{2\rho_0} C_{ijkl}\varepsilon_{ij}\varepsilon_{kl} - \frac{\left(T - T_0\right)}{\rho_0}\beta_{ij}\varepsilon_{ij} - \frac{\varepsilon_l \xi_s E_s V_s \varepsilon_{11}}{\rho_0} + V_s \frac{\lambda}{T^*}\left(T - T^*\right)\xi \\ & + C_E\left[\left(T - T_0\right) - T\ln\left(\frac{T}{T_0}\right)\right]\end{aligned} \tag{5}$$

where, C_{ijkl}, β_{ij}, ε_l, ξ_s, E_s, V_s, λ, T^*, C_E, and T_0 are the elasticity tensor, stress-temperature coupling coefficients tensor, maximum recoverable strain, stress induced martensite volume fraction, modulus of the SMA, SMA volume fraction of the hybrid composite, latent heat of phase transformation, critical temperature, specific heat of material, and initial temperature, respectively. On the other hand, by differentiating Eq. (5) with respect to the strain components, Brinson's constitutive law of the SMA may be obtained. For the special case where the martensite volume fraction is zero, Eq. (5) reduces to the generalized coupled thermoelasticity expressions proposed by Hetnarski and Eslami [13]. Comparing Eqs. (3) and (5), the transformation force and entropy may be written in the following explicit forms:

$$\Lambda = -\rho_0 \frac{\partial \psi}{\partial \xi} = \varepsilon_l E_s k_s \varepsilon_{11} - \rho_0 V_s \frac{\lambda}{T^*}\left(T - T^*\right) \tag{6}$$

$$\eta = -\frac{\partial \psi}{\partial T} = \frac{\beta_{ij}\varepsilon_{ij}}{\rho_0} - V_s \frac{\lambda}{T^*}\xi + C_E \ln\left(\frac{T}{T_0}\right) \tag{7}$$

The second term of the last side of Eq. (7), i.e., $V_s \frac{\lambda}{T^*}\xi$ has not been appeared in other researches. The rate form of the entropy may be written as follows:

$$\dot{\eta} = \frac{\beta_{ij}\dot{\varepsilon}_{ij}}{\rho_0} - V_s \frac{\lambda}{T^*}\dot{\xi} + C_E \frac{\dot{T}}{T} \tag{8}$$

Since it is intended to present a general coupled thermoelasticity analysis, the first term of the right hand side of Eq. (8), i.e., $\beta_{ij}\dot{\varepsilon}_{ij}/\rho_0$ is retained [13,14]. The final form of the energy balance equation (4) may be rewritten as:

$$q_{i,i} - \left(\varepsilon_l E_s \varepsilon_{11} + \rho_0 \lambda\right) V_s \dot{\xi} + T\beta_{ij}\dot{\varepsilon}_{ij} + \rho_0 C_E \dot{T} = 0 \tag{9}$$

Eq. (9) implies that the volumetric rate of the martensite phase transformation and the dilatation rate are main sources of the internal heat generation within the shape memory wires. The constitutive equation of the *i*th layer of the plate in the principal coordinates of the material properties (fiber axes) may be written as:

$$\tilde{\boldsymbol{\sigma}} = \hat{\mathbf{Q}}\left(\tilde{\boldsymbol{\varepsilon}} - \tilde{\boldsymbol{\varepsilon}}_T\right) \tag{10}$$

where

$$\tilde{\sigma} = \begin{Bmatrix} \sigma_1 \\ \sigma_2 \\ \tau_{12} \\ \tau_{13} \\ \tau_{23} \end{Bmatrix}, \qquad \tilde{\varepsilon} = \begin{Bmatrix} \varepsilon_1 \\ \varepsilon_2 \\ \gamma_{12} \\ \gamma_{13} \\ \gamma_{23} \end{Bmatrix}, \qquad \tilde{\varepsilon}_T = \begin{Bmatrix} \alpha_1 \\ \alpha_2 \\ 0 \\ 0 \\ 0 \end{Bmatrix} \Delta T \tag{11}$$

and the subscripts 1, 2, and 3 correspond to the fiber direction, in-plane transverse direction of the fiber and out-of plane transverse direction of the fiber, respectively and σ, τ, ε, and γ are normal stress, shear stress, and normal and shear strains, respectively. $\tilde{\boldsymbol{\varepsilon}}_T$ is the thermal strains vector in the principal coordinates of the material. The non-zero elements of the stiffness matrix $\hat{\mathbf{Q}}$ are:

$$\hat{Q}_{11} = \frac{E_1}{1-\nu_{12}\nu_{21}},\ \hat{Q}_{22} = \frac{E_2}{1-\nu_{12}\nu_{21}},\ \hat{Q}_{12} = \hat{Q}_{21} = \frac{\nu_{12}E_2}{1-\nu_{12}\nu_{21}},\ \hat{Q}_{33} = G_{12},\ \hat{Q}_{44} = G_{13},\ \hat{Q}_{55} = G_{23} \tag{12}$$

E, ν, and *G* are Young's modulus, Poisson's ratio, and shear modulus, respectively. Based on Brinson's constitutive equation of the shape memory alloy [15], the stress and strain quantities may be related through the martensite volume fraction (ξ) as:

$$\sigma - \sigma_0 = E(\xi)\varepsilon - E(\xi_0)\varepsilon_0 + \Omega(\xi)\xi_s - \Omega(\xi_0)\xi_{s0} + \Theta(T - T_0), \qquad \xi = \xi_s + \xi_T \tag{13}$$

where, Ω is the transformation tensors and ξ_s and ξ_T represent the stress- and temperature-induced martensite volume fractions, respectively. The subscript *0* denotes the initial quantities of the local or global event under investigation. The Young's modulus of elasticity of the SMA is dependent on the martensite and austenite moduli:

$$E(\xi) = E_A + \xi(E_M - E_A),\ \Omega(\xi) = -\varepsilon_l E(\xi) \tag{14}$$

Where E_A and E_M are Young's moduli of the austenite and martensite phases and the martensite volume fraction may be determined based on the following kinetic laws of transformation:
(i) Conversion from the austenite to the de-twinned martensite phase:

In this case: $\sigma_s^{cr}+C_M\left(T-M_s\right)<\sigma<\sigma_f^{cr}+C_M\left(T-M_s\right)$ and $T>M_s$:

$$\xi_s=\frac{1-\xi_{s0}}{2}\times\cos\left\{\frac{\pi}{\sigma_s^{cr}-\sigma_f^{cr}}\left[\sigma-\sigma_f^{cr}-C_M\left(T-M_s\right)\right]\right\}+\frac{1+\xi_{s0}}{2}$$
$$\xi_T=\xi_{T0}-\frac{\xi_{T0}}{1-\xi_{s0}}\left(\xi_s-\xi_{s0}\right) \tag{15}$$

(ii) Conversion from de-twinned martensite to austenite phase:

For $T>A_s$ and $C_A\left(T-A_f\right)<\sigma<C_A\left(T-A_s\right)$

$$\xi=\frac{\xi_0}{2}\times\left\{\cos\left[\frac{\pi}{A_f-A_s}\left(T-A_s-\frac{\sigma}{C_A}\right)\right]+1\right\}$$
$$\xi_s=\xi_{s0}-\frac{\xi_{s0}}{\xi_0}\left(\xi_0-\xi\right),\qquad \xi_T=\xi_{T0}-\frac{\xi_{T0}}{\xi_0}\left(\xi_0-\xi\right) \tag{16}$$

In Eq. (15), σ_s^{cr} and σ_f^{cr} are the critical stresses associated with the start and finish of the phase transformation process, respectively. A_s, A_f, and M_s correspond to the start and finishing temperatures of the austenite phase transformation and temperature of the start of the martensite transformation, respectively. C_M and C_A are the zero-stress slopes of the transformation regions into martensite and into austenite phases, respectively. Eq. (10) may be modified for a layer with embedded SMA wires, as:

$$\tilde{\boldsymbol{\sigma}}=\hat{\mathbf{Q}}\left(\tilde{\boldsymbol{\varepsilon}}-\tilde{\boldsymbol{\varepsilon}}_T\right)-\tilde{\boldsymbol{\sigma}}^{\mathrm{s}} \tag{17}$$

where,

$$\tilde{\boldsymbol{\sigma}}^{\mathrm{s}}=\left\langle V_sE_s\xi\varepsilon_L\quad 0\quad 0\quad 0\quad 0\right\rangle \tag{18}$$

Since it is assumed that the SMA wires are parallel to the composite fibers, the following relations may be used to determine the effective material properties for each layer in the principal directions of the fibers, using the micromechanical relations appeared in Eq. (1).

$$E_1=E_{1c}V_c+E_sV_s\ ,\quad E_2=\frac{E_{2c}E_s}{V_cE_s+V_sE_{2c}},\quad G_{12}=\frac{G_{12c}G_s}{V_cG_s+V_sG_{12c}},\quad G_{13}=\frac{G_{13c}G_s}{V_cG_s+V_sG_{13c}},$$
$$\nu_{12}=\nu_{12c}V_c+\nu_sV_s,\quad \rho=\rho_cV_c+\rho_sV_s,\qquad \alpha_1=\alpha_{1c}V_c+\alpha_sV_s\ ,\qquad \alpha_2=\frac{\alpha_{2c}\alpha_s}{\alpha_{2c}V_s+\alpha_sV_c} \tag{19}$$

where, the subscripts *s* and *c* stand for the SMA and composite materials, respectively.

2.3 The refined constitutive and contact laws

Hertz contact law has been used by almost all researchers for impact analysis of plates and shells. Turner [16] has revised this law for a transversely isotropic plate impacted by a rigid spherical indenter, as follows:

$$F_c=k_c\alpha^{3/2} \tag{20}$$

where

$$k_c = \frac{4}{3} E_c \sqrt{R}$$

$$E_c = \frac{2\sqrt{2} G_{xy}}{1 - \nu_{xy} \sqrt{\frac{E_x / E_y - \nu_{xz}^2}{1 - \nu_{xy}^2}} + \sqrt{\frac{E_x / E_y - \nu_{xz}^2}{1 - \nu_{xy}^2}} \frac{1 + \left(E_x / 2G_{xz} - 1\right) - \nu_{xz}\left(1 + \nu_{xy}\right)}{1 - \nu_{xy}^2}} \tag{21}$$

where, α, k_c and E_c are the indentation value, apparent contact stiffness, and effective apparent modulus, respectively. For the unloading phase, the modified Hertzian contact law proposed by Yang and Sun [17] is employed in the present research:

$$F_c = F_{max} \left(\frac{\alpha - \alpha_0}{\alpha_{max} - \alpha_0} \right)^{\frac{5}{2}} \tag{22}$$

where, F_{max} is the maximum contact force reached during the impact, α_{max} is the maximum indentation corresponds to F_{max} and α_0 is the permanent indentation, if any.

2.4 The nonlinear governing equations of motion

The displacement field of the plate may be described based on the first-order shear-deformation theory:

$$\begin{aligned} u(x, y, z, t) &= u_0(x, y, t) + z\varphi_x(x, y, t), \\ v(x, y, z, t) &= v_0(x, y, t) + z\varphi_y(x, y, t), \\ w(x, y, z, t) &= w_0(x, y, t) \end{aligned} \tag{23}$$

where u_0, v_0, w_0, φ_x, and φ_y are displacement components of the mid-layer of the plate in the *x*, *y*, and *z*-directions, and rotations of the cross section of the plate, respectively. Since the *z*-dependency of the displacement components is pre-defined, a 2D mesh composed of 8-node quadratic elements [18] may be employed to trace the in-plane variations of the displacement parameters of Eq. (30):

$$\boldsymbol{\delta}(x, y, z, t) = \begin{Bmatrix} \mathrm{u} \\ \mathrm{v} \\ \mathrm{w} \end{Bmatrix} = \begin{bmatrix} \mathbf{N} & \mathbf{0} & \mathbf{0} & z\mathbf{N} & \mathbf{0} \\ \mathbf{0} & \mathbf{N} & \mathbf{0} & \mathbf{0} & z\mathbf{N} \\ \mathbf{0} & \mathbf{0} & \mathbf{N} & \mathbf{0} & \mathbf{0} \end{bmatrix} \begin{Bmatrix} \mathbf{U} \\ \mathbf{V} \\ \mathbf{W} \\ \Phi_{\mathbf{x}} \\ \Phi_{\mathbf{y}} \end{Bmatrix} = \hat{\mathbf{N}}\,\mathbf{D} \tag{24}$$

where **N** and **D** are the shape function matrix and vector of the nodal values of the displacement parameters (u_0, v_0, w_0, φ_x, and φ_y), respectively. Cauchy's strain-displacement relations are:

$$\boldsymbol{\varepsilon}=\begin{bmatrix} \frac{\partial}{\partial x} & 0 & 0 \\ 0 & \frac{\partial}{\partial y} & 0 \\ \frac{\partial}{\partial y} & \frac{\partial}{\partial x} & 0 \\ \frac{\partial}{\partial z} & 0 & \frac{\partial}{\partial x} \\ 0 & \frac{\partial}{\partial z} & \frac{\partial}{\partial y} \end{bmatrix}\boldsymbol{\delta}=\mathbf{D}\,\widehat{\mathbf{N}}\,\mathbf{D}\;=\boldsymbol{\Xi}\mathbf{D} \tag{25}$$

Assuming a general parabolic transverse temperature for the composite plate with embedded SMA wires, the temperature rise field may be described as

$$\theta^{*}(x,y,z,t)=\theta_0(x,y,t)+z\theta_1(x,y,t)+z^2\theta_2(x,y,t)=\begin{bmatrix}\mathbf{N} & z\mathbf{N} & z^2\mathbf{N}\end{bmatrix}\begin{Bmatrix}\boldsymbol{\Theta}_0\\ \boldsymbol{\Theta}_1\\ \boldsymbol{\Theta}_3\end{Bmatrix}=\mathbf{H}\,\boldsymbol{\Theta} \tag{26}$$

The governing equations may be derived using a Galerkin-type method. In this regard, residues of the energy balance Eq. (9) and the equation of motion in terms of the stress components (in absence of the body forces) may be multiplied respectively, by variations of the temperature and displacement components in the integrals of the weighted residuals, as follows:

$$\begin{gathered}\int_V\left[q_{i,i}-\left(\varepsilon_l E_s\varepsilon_{11}+\rho_0\lambda\right)V_s\dot{\xi}+T\beta_{ij}\dot{\varepsilon}_{ij}+\rho_0 C_E\dot{T}\right]\delta\theta^{*}dV=0\\ \int_V\left(\sigma_{ij,j}-\rho\ddot{u}_i\right)\delta u_i dV=0,\qquad i=1,2,3\end{gathered} \tag{27}$$

Combining the two equations appeared in Eq. (27) and integrating by parts, leads to:

$$\begin{gathered}\int_V\left[-\left(\varepsilon_l E_s\varepsilon_{11}+\rho_0\lambda\right)V_s\dot{\xi}+T\beta_{ij}\dot{\varepsilon}_{ij}+\rho_0 C_E\dot{\theta}^{*}\right]\delta\theta^{*}dV-\int_V q_i\delta\theta^{*}{}_{,i}dV+\int_V\sigma_{ij}\delta\varepsilon_{ij}dV=\\ -\int_A q_i n_i\delta\theta^{*}dA+\int_A\sigma_{ij}n_j\delta u_i dA+\int_V\left(X_i-\rho\ddot{u}_i\right)\delta u_i dV\end{gathered} \tag{28}$$

Eq. (28) may be rewritten based on Fourier's heat transfer law and performing some manipulations, as follows:

$$\begin{gathered}\int_V\rho_0 C_E\dot{\theta}^{*}\delta\theta^{*}dV-\int_V\varepsilon_l E_s V_s\varepsilon_{11}\dot{\xi}\delta\theta^{*}dV+\int_V T\beta_{ij}\dot{\varepsilon}_{ij}\delta\theta^{*}dV-\int_V\rho_0 V_s\lambda\dot{\xi}\delta\theta^{*}dV+\int_V k_{ij}\theta^{*}{}_{,j}\delta\theta^{*}{}_{,i}dV\\ +\int_V\sigma_{ij}\delta\varepsilon_{ij}dV+\int_V\rho\ddot{u}_i\delta u_i dV=-\int_A q_i n_i\delta\theta^{*}dA+\int_A\sigma_{ij}n_j\delta u_i dA\end{gathered} \tag{29}$$

Since $\int_V(\cdots)dV=\int_{\mathrm{A}}\int_{-\frac{h}{2}}^{\frac{h}{2}}(\cdots)dzd\mathrm{A}$ (A is the mid-surface area of the plate), the finite element form of Eq. (29) may be written in the following form:

$$\begin{aligned}
&\delta\mathbf{D}^{T}\int_{\mathrm{A}}\int_{-\frac{h}{2}}^{\frac{h}{2}}\left[\rho\hat{\mathbf{N}}^{T}\hat{\mathbf{N}}\ddot{\mathbf{D}}+\boldsymbol{\Xi}^{T}\mathbf{Q}\,\boldsymbol{\Xi}\mathbf{D}\right]dz\mathrm{d}\mathrm{A}+(\dot{\mathbf{D}})\delta\boldsymbol{\Theta}^{T}\int_{\mathrm{A}}\int_{-\frac{h}{2}}^{\frac{h}{2}}T\mathbf{H}^{T}\boldsymbol{\beta}\boldsymbol{\Xi}\dot{\mathbf{D}}\,dz\mathrm{d}\mathrm{A}\\
&+\delta\boldsymbol{\Theta}^{T}\int_{\mathrm{A}}\int_{-\frac{h}{2}}^{\frac{h}{2}}\left[\left(\left[\rho_0 C_E\mathbf{H}^{T}\mathbf{H}\dot{\boldsymbol{\Theta}}+k_{ij}\mathbf{H}_{,i}^{T}\mathbf{H}_{,j}\boldsymbol{\Theta}\right]-\varepsilon_l E_s V_s\dot{\xi}\mathbf{H}^{T}\begin{bmatrix}1&0&0&0&0\end{bmatrix}\boldsymbol{\Xi}\mathbf{D}\right)\right.\\
&\left.+h\mathbf{H}^{T}\mathbf{H}\boldsymbol{\Theta}\right]dz\mathrm{d}\mathrm{A}\Big\}=\delta\boldsymbol{\Theta}^{T}\int_{\mathrm{A}}\left\{\int_{-\frac{h}{2}}^{\frac{h}{2}}\rho_0 V_s\lambda\dot{\xi}\mathbf{H}^{T}dz-\left[q_n+h^{*}\left(T_{initial}-T_{\infty}\right)\right]\mathbf{H}^{T}\right\}d\mathrm{A}\\
&+\delta\mathbf{D}^{T}\int_{\mathrm{A}}\int_{-\frac{h}{2}}^{\frac{h}{2}}\boldsymbol{\Xi}^{T}\left[\mathbf{Q}\boldsymbol{\varepsilon}_T+\boldsymbol{\sigma}^{s}\right]dz\mathrm{d}\mathrm{A}+F_c\delta w_i
\end{aligned}\tag{30}$$

where Γ is the heat transfer boundary. Indeed, both the heat conduction and heat convection fluxes are considered in the present research (h^{*} is heat convection coefficient of the top/bottom surface of the plate). F_c and w_i are respectively the contact force and vertical displacement of the indenter. Eq. (30) may be represented by the following compact form:

$$\delta\mathbf{W}^{T}\left[\mathbf{M}\ddot{\mathbf{W}}+\mathbf{C}\left(\mathbf{W},\dot{\mathbf{W}}\right)\dot{\mathbf{W}}+\mathbf{K}\left(\mathbf{W},\dot{\mathbf{W}}\right)\mathbf{W}-\mathbf{F}\left(\mathbf{W},\dot{\mathbf{W}}\right)\right]=0\tag{31}$$

where $\mathbf{W}$ is the augmented matrix of the nodal values of the coupled unknown parameters

$$\begin{Bmatrix}u\\v\\w\\\theta^{*}\end{Bmatrix}=\begin{bmatrix}\hat{\mathbf{N}}&\mathbf{0}\\\mathbf{0}&\mathbf{H}\end{bmatrix}\begin{Bmatrix}\mathbf{D}\\\boldsymbol{\Theta}\end{Bmatrix}=\mathbf{B}\mathbf{W}\tag{32}$$

The non-linear coupled governing equations of motion may be derived from Eq. (30), based on the fact that Eq. (31) must hold for any arbitrary choice of $\delta\mathbf{W}\neq\mathbf{0}$:

$$\mathbf{M}\ddot{\mathbf{W}}+\mathbf{C}\left(\mathbf{W},\dot{\mathbf{W}}\right)\dot{\mathbf{W}}+\mathbf{K}\left(\mathbf{W},\dot{\mathbf{W}}\right)\mathbf{W}=\mathbf{F}\left(\mathbf{W},\dot{\mathbf{W}}\right)\tag{33}$$

Matrices $\mathbf{C}$, $\mathbf{K}$, and $\mathbf{F}$ are functions of the strain-rate, martensite volume fraction, and temperature distribution and rise. The strain-rate and martensite volume fractions are in turn dependent on displacements and relative velocities of the individual points of the plate. The system of Eq. (33) has to be assembled with the governing equation of motion of the indenter. Based on Newton's second law and Eq. (20):

$$\begin{aligned}
&m_i\ddot{w}_i+k_c\left(w_i-w_c\right)^{\frac{3}{2}}=0\\
&F_c=k_c\left(w_i-w_c\right)^{\frac{3}{2}}
\end{aligned}\tag{34}$$

m_i and w_c are the mass of the indenter and lateral deflection of the impacted node of the plate, respectively. Therefore, Eq. (31) may be augmented by adding a row corresponding to Eq. (34), in addition to augmentation of the whole nodal parameters vector by adding the w_i degree of freedom. The resulting system of equations is solved iteratively within each time step, using a return-mapping [19] Newton-Raphson algorithm that is especially used to solve the non-linear constitutive equation of the SMA. Because the SMA stress is different from the plate stress, the following bridging tensor [20] relations are used to extract the true stress of SMA which directly effects the phase transformation process:

$$\sigma = \frac{1}{c_{11}}\sigma_{xx} - \frac{c_{12}}{c_{11}c_{22}}\sigma_{yy}$$

$$c_{11} = V_s + V_m b_{11} + V_f \frac{b_{11}}{a_{11}}, \quad c_{12} = V_m b_{12} + V_f \frac{b_{12}}{a_{11}} - V_f \frac{a_{12}b_{22}}{a_{22}a_{11}}, \quad c_{22} = V_s + V_m b_{22} + V_f \frac{b_{22}}{a_{22}},$$

$$a_{11} = \frac{E_m}{E_f}, \quad a_{22} = \frac{1}{2}\left(1 + \frac{E_m}{E_f}\right), \; a_{33} = \frac{1}{2}\left(1 + \frac{G_m}{G_f}\right), \quad a_{12} = \frac{-\frac{V_f}{E_1^f} + \frac{V_m}{E_1^f}}{\frac{1}{E_1^f} - \frac{1}{E_1^m}}(a_{11} - a_{22}), \tag{35}$$

$$b_{11} = \frac{E_m}{E_s}, \; b_{22} = \frac{1}{2}\left(1 + \frac{E_m}{E_s}\right), \quad b_{33} = \frac{1}{2}\left(1 + \frac{G_m}{G_s}\right), \quad b_{12} = \frac{-\frac{V_s}{E_1^s} + \frac{V_m}{E_1^m}}{\frac{1}{E_1^s} - \frac{1}{E_1^m}}(b_{11} - b_{22})$$

where V_s, V_m and V_f are volume fractions of the SMA, matrix and fiber, respectively. a_{ij}, b_{ij} and c_{ij} are coefficients of the bridging tensor and σ is the transformation stress of the SMA wire. In this procedure, the residue may be defined based on Eq. (13) and the bridging tensor coefficients:

$$R = \frac{1}{c_{11}}\sigma_{xx} - \frac{c_{12}}{c_{11}c_{22}}\sigma_{yy} - \sigma \tag{36}$$

So that the tangent stiffness matrix ($\boldsymbol{K_T}$) and increment of the unknown stress of an arbitrary nodal point may be defined as follows:

$$\boldsymbol{K_T} = \left.\frac{\partial \mathrm{R}}{\partial \sigma}\right|_{\sigma}, \qquad \Delta\sigma = -\boldsymbol{K_T}^{-1}\mathrm{R} \tag{37}$$

Therefore,

$$\boldsymbol{K_T} = \frac{\left(\frac{\partial(\sigma_{xx})}{\partial\sigma}c_{11} - \frac{\partial(c_{11})}{\partial\sigma}\sigma_{xx}\right)}{c_{11}^2} - \frac{\left[\left(\frac{\partial(\sigma_{yy})}{\partial\sigma}c_{12} + \frac{\partial(c_{12})}{\partial\sigma}\sigma_{yy}\right)c_{11}c_{22} - \left(\frac{\partial(c_{11})}{\partial\sigma}c_{22} + \frac{\partial(c_{22})}{\partial\sigma}c_{11}\right)c_{12}\sigma_{yy}\right]}{(c_{11}c_{22})^2} - 1 \tag{38}$$

The stress value at the *k*th iteration may be determined from:

$$\sigma^{k+1} = \sigma^k + \Delta\sigma \tag{39}$$

The expanded forms of the partial differentiations appeared in Eq. (38) are:

$$\frac{\partial c_{11}}{\partial\sigma} = \frac{\partial b_{11}}{\partial\sigma}\left(V_m + \frac{V_f}{a_{11}}\right), \quad \frac{\partial c_{12}}{\partial\sigma} = \frac{\partial b_{12}}{\partial\sigma}\left(V_m + \frac{V_f}{a_{11}}\right) - \frac{\partial b_{22}}{\partial\sigma}\frac{a_{12}V_f}{a_{22}a_{11}},$$

$$\frac{\partial c_{22}}{\partial\sigma} = \frac{\partial b_{22}}{\partial\sigma}\left(V_m + \frac{V_f}{a_{22}}\right), \quad \frac{\partial(\sigma_{xx})}{\partial\sigma} = \frac{\partial Q_{11}}{\partial\sigma}(\varepsilon_{xx} - \alpha_{xx}\Delta T) + \frac{\partial Q_{12}}{\partial\sigma}(\varepsilon_{yy} - \alpha_{yy}\Delta T) - k_s\varepsilon_l\frac{\partial(E_s\xi_s)}{\partial\sigma}$$

$$\frac{\partial(\sigma_{yy})}{\partial\sigma} = \frac{\partial Q_{12}}{\partial\sigma}(\varepsilon_{xx} - \alpha_{xx}\Delta T) + \frac{\partial Q_{22}}{\partial\sigma}(\varepsilon_{yy} - \alpha_{yy}\Delta T) \tag{40}$$

$$\frac{\partial(E_s\xi_s)}{\partial\sigma} = \frac{\partial\xi}{\partial\sigma}(E_m - E_a)\xi_s + \frac{\partial\xi_s}{\partial\sigma}E_s, \quad \frac{\partial(E_s)}{\partial\sigma} = \frac{\partial\xi}{\partial\sigma}(E_m - E_a)$$

and, based on Eqs. (15) and (16):

(i) For conversion from the austenite to the de-twinned martensite phase:

$$\frac{\partial \xi_{\mathrm{s}}}{\partial \sigma}=\frac{1-\xi_{s0}}{2}\left[\frac{-\pi}{\sigma_s^{cr}-\sigma_f^{cr}}\sin\left\{\frac{\pi}{\sigma_s^{cr}-\sigma_f^{cr}}\left[\sigma-\sigma_f^{cr}-C_M\left(T-M_s\right)\right]\right\}\right]$$
$$\frac{\partial \xi_{\mathrm{T}}}{\partial \sigma}=-\frac{\xi_{T0}}{1-\xi_{s0}}\frac{\partial \xi_{\mathrm{s}}}{\partial \sigma},\quad \frac{\partial \xi}{\partial \sigma}=\frac{\partial \xi_{\mathrm{s}}}{\partial \sigma}+\frac{\partial \xi_{\mathrm{T}}}{\partial \sigma} \tag{41}$$

(ii) For conversion from de-twinned martensite to austenite phase:

$$\frac{\partial \xi}{\partial \sigma}=\frac{\xi_0}{2}\frac{\pi}{\left(A_f-A_{\mathrm{s}}\right)C_A}\sin\left[\frac{\pi}{A_f-A_{\mathrm{s}}}\left(T-A_{\mathrm{s}}-\frac{\sigma}{C_A}\right)\right],\quad \frac{\partial \xi_{\mathrm{s}}}{\partial \sigma}=\frac{\xi_{s0}}{\xi_0}\frac{\partial \xi}{\partial \sigma} \tag{42}$$

3 The proposed solution algorithm

In the present research, the following steps are employed to solve the highly non-linear and piece-wise defined governing equations:

(1) The reference plane of the plate is discretized into second-order quadrilateral elements.
(2) The element matrices are assembled.
(3) The boundary conditions are incorporated and the initial values are defined.
(4) The solution time interval is divided into time steps that are much smaller than the contact time of the plate.
(5) Using the modified Brinson's model, the transformation-rates, and the temperature distribution to establish the stiffness and force matrices.
(6) The non-linear coupled augmented time-dependent system of equations of the unknown nodal parameters is solved using the second-order Runge-Kutta numerical time integration method.
(7) The martensite volume fraction, its rate, and the temperature rises are determined.
(8) The material properties are updated based on the determined transformation-rates and temperature rises.
(9) The apparent contact stiffness is updated.
(10) The damping, stiffness, and force matrices of the entire plate are updated.
(11) The algorithm presented by Shariyat and Ghaznavi [12] may be used to check whether a global, local, or reverse loading/unloading event is in process.
(12) When ($T < M_s$) the shape memory effects are dominant, and the unloading path (in the stress-strain plane) exhibits a ferroelastic behavior. Tension-compression hysteresis loops obtained in low temperatures, are called ferroelastic loops [21,22]. In general, the material behavior of SMAs and other ferroelastics is nonlinear, hysteretic, and temperature-dependent. In the present analysis, this behavior is modeled based on a kinematic hardening plasticity model using the backlash concept.
(13) Items 6 to 13 are repeated until solutions corresponding to the current time step converge. For example, the convergence criterion may be chosen as:

$$\left|\frac{\left\|\mathbf{S}_i^{\,k}-\mathbf{S}_i^{\,k-1}\right\|}{\left\|\mathbf{S}_i^{\,k}\right\|}\right|\le 10^{-4} \tag{43}$$

where *k* is the iteration number of the *i*th time step and $\mathbf{S}$ is the augmented vector of the nodal parameters of the entire plate:

$$\mathbf{S} = \begin{Bmatrix} \mathbf{W} \\ w_i \end{Bmatrix} \tag{44}$$

(14) The displacement, velocity, acceleration, stress, transformation-rate, and temperature results are stored to be used as initial conditions for the next time step.

(15) Items 6 to 15 are repeated for the next time step until the final analysis time is reached.

4 Results and discussions

Based on a convergence analysis whose results are not included here due to length restriction of the paper, a 8×8 mesh size has led to convergent results; so that all the results have been extracted based on this mesh size. Moreover, an integration time step in the order of 10^{-5} (sec) that is much less than the response time of the structure is adopted to accurately trace the time history of the displacement parameters.

4.1 Verification of the results by the experimental data

In order to verify the finite element code that was written in MATLAB environment, four rectangular composite plates with and without SMA wires, were prepared and subjected to impact tests. Mechanical properties of the composite plates with woven E-glass fiber and epoxy matrix were determined according to ASTM D3518 and ASTM D3039 test standards. The tension test samples and apparatus are shown in Figures (2) and (3), respectively.

The Glass/epoxy composite plate is composed of five layers with identical thicknesses and total thickness of 2mm. Woven IRGWP200 ‘E’ glass fibers, a CY219 epoxy resin matrix, and a HY5161 hardener were employed to fabricate the composite laminates. The volume fraction of the glass fibers was approximately 59%. The impact test was performed using an instrumented falling weight testing machine with no energy storage device [Figure (4)] and the maximum impact energy was limited by the adjustable falling height and the fixed mass of the steel indenter. In accordance with ASTM D 3029 standard, a batch of square, thin (140 mm side and 2 mm thick) specimens is clamped in a fixture with a square slot of 100mm. The test samples are shown in Figure (5).

The indenter has a hemispherical head of 8 mm radius and a 2.685 kg mass; the piezoelectric load cell is placed at the other extremity of the calibrated cylindrical rod that constitutes the dart, at which the pushing mass is connected. Figure (6) shows the specimen clamping apparatus. The dart was released from a height of 0.2m. The vertical guides of the impact tower were lubricated frequently to minimize any friction that may be generated during the descent of the indenter. The E-glass composite specimens were subjected to an impact with a 1.981 m/sec velocity.

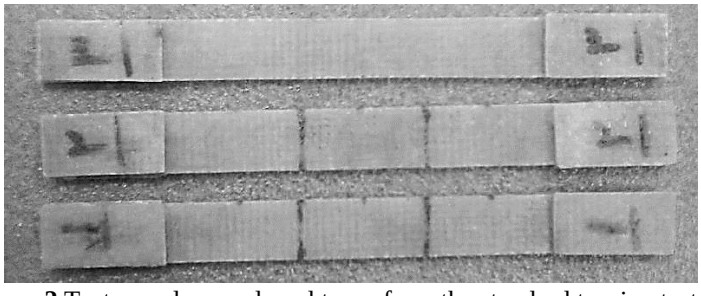

Figure 2 Test samples employed to perform the standard tension tests.

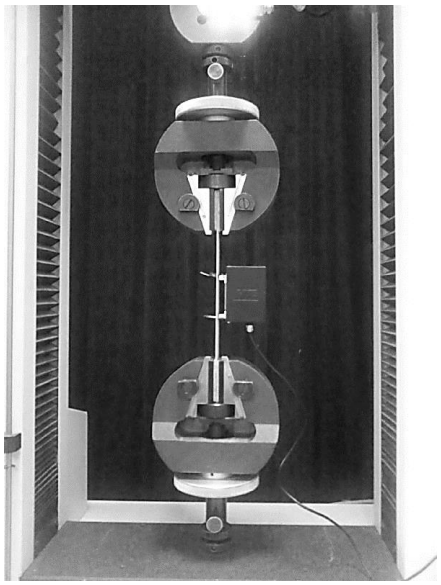

Figure 3 The composite tension test apparatus

Figure 4 The drop test apparatus

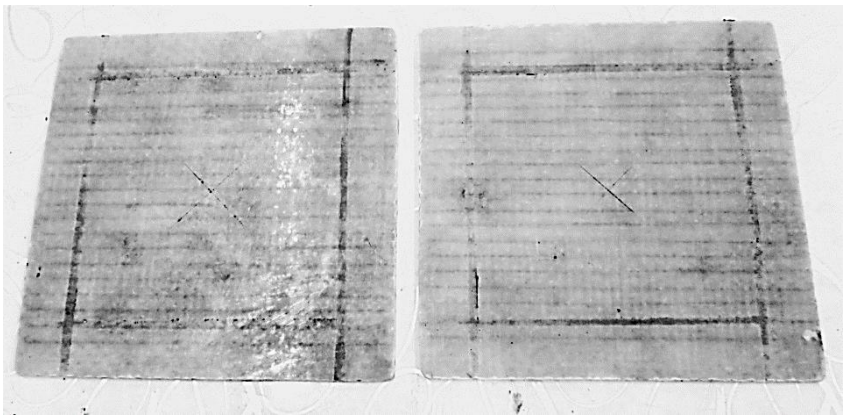

Figure 5 Impact test specimens

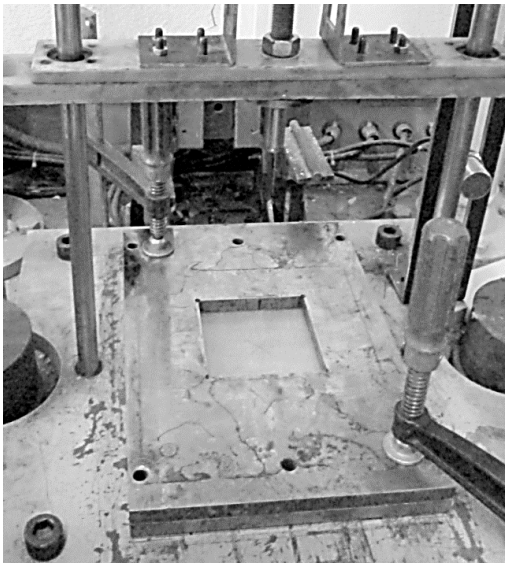

Figure 6 Fixture of the impact specimen

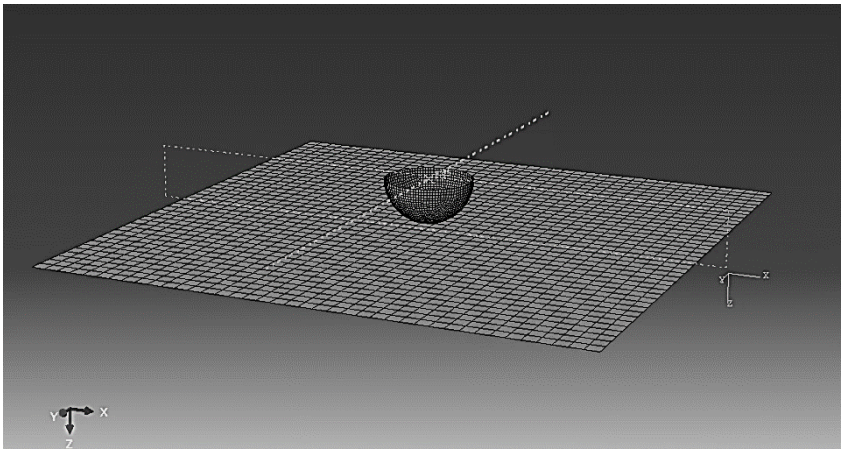

Figure 7 Simulation of the impact test with ABAQUS 6.12

In order to present an adequate verification for the written MATLAB FEM code, an extra simulation was performed by using the commercial finite element ABAQUS 6.12 code. The resulting FEM model in ABAQUS is shown in Figure (7). The experimental data of the impact test are compared with MATLAB and ABAQUS results [Figure (8)]. Results are verified for a composite plate without SMA wires.

The time history of the contact force predicted by present formulation are compared in Figure (8) with that of ABAQUS and the experimental results. As may readily be noted, there is a good agreement among the results. Moreover, time history of the lateral deflection of the central point of the plate is compared in Figure (9) with that of ABAQUS and once again, a good concordance is noticed between the results.

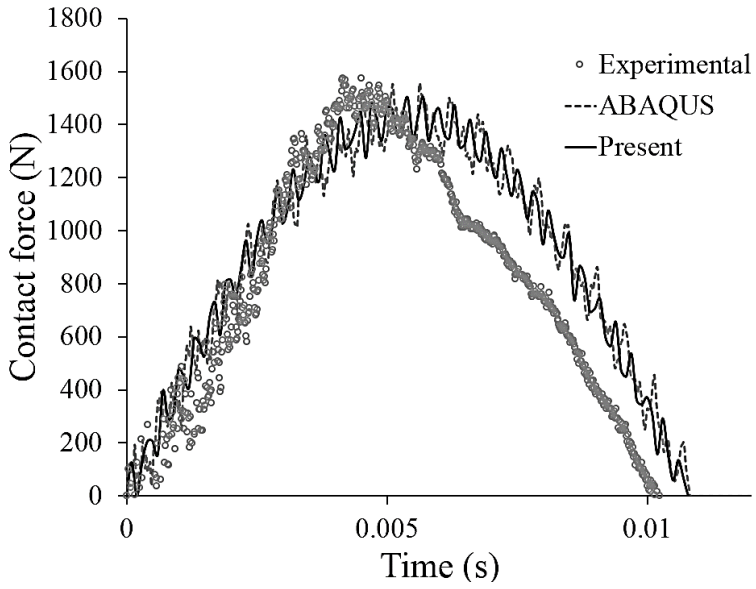

Figure 8 A comparison among the predicted time histories of the contact force for a composite plate without SMA wires.

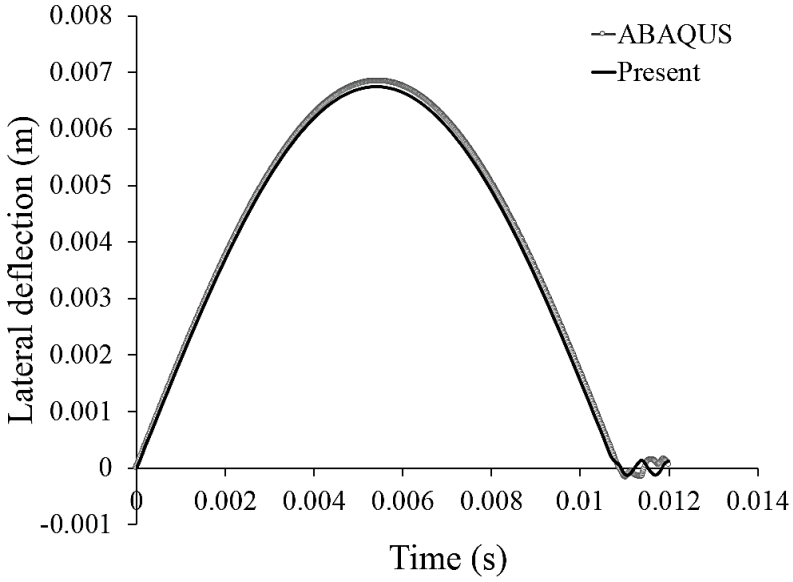

Figure 9 A comparison between the predicted time histories of the lateral deflection of the plate without SMA wires.

4.2 Effects of the initial temperature

To present a comprehensive parametric study, a cross-ply [0/90/0/90/0] laminated Epoxy/Glass composite plate with embedded SMA wires with the following specifications is chosen:

Composite plate: $E_1 = 38.2GPa,\quad E_2 = E_3 = 9.56GPa,\quad G_{12} = G_{13} = 3.44GPa,$

$$\nu_{12} = \nu_{13} = \nu_{23} = 0.2850,\ \rho = 1540kgm^{-3},\ K = 3.46\ W/mK,\ \alpha = 5\times10^{-6}\,C^{-1}$$

SMA wires: $E_A = 67GPa,\quad E_M = 26.3GPa,\quad \nu_A = \nu_M = 0.3,\quad \rho = 6450kgm^{-3},\quad A_s = 34.5C,$
$A_f = 49C,\ M_s = 18.4C,\ M_f = 9C,\ C_A = 13.8MPa/C,\quad C_M = 8MPa/C,$
$\varepsilon_L = 0.063,\ K = 18\,W/mK,\quad \alpha = 9\times10^{-6}C^{-1},\quad \lambda = 18914\ J/kg$

The SMA wires are assumed to be embedded in the top and bottom layers of the composite plate and constitute 50% of the volume of the mentioned layers. Dimensions of the plate are 100mm×100mm×5mm. The 6.8 kg steel indenter is assumed to have an initial velocity of 5 m/s and a hemispherical head with a 6.35 mm radius.

The austenite phase is stiffer than the martensite phase. Therefore, depending on the initial temperature, the material may consist of martensite, austenite or a mixture of them. Below the austenite start temperature, the SMA exhibits a ferroelastic behavior. In the present research, a kinematic hardening model with backlash is employed to model the ferroelastic behavior of the SMA. In order to investigate influence of the initial temperature of the SMA, 10 different initial temperatures ranging from 0 to 50C are chosen in the sensitivity analysis. The relevant time histories of the contact force are illustrated in Figure (10).

Since the transformation stresses grow with temperature, in addition to the martensite to austenite phase transformation, the contact force increases in higher temperatures.

Consequently, the response time, i.e., the contact time, decreases in higher initial temperatures. The resulting time histories of the lateral deflection of the plate are depicted in Figure (11). This figure reveals that the lateral deflection of the plate increases by decreasing the initial temperatures. Furthermore, as Figure (11) shows, magnitude of the lateral deflection of the plate after the impact may not become zero, for some initial temperatures. Indeed, when $T_0<A_s$, the plate undergoes residual strains [19] and cannot retain its initial geometry. When the temperature of the SMA wire is higher than A_s, the SMA wire transforms to austenite in the unloading process whereas, when the temperature is below the mentioned temperature, the SMA wire cannot accomplish a reverse transformation; so that, some residual strains remain in the wire.

If the SMA wire is embedded in a composite plate, the plate tends to retain its initial configuration after impact, through exerting a compressive stress on the wires; a phenomenon that affects magnitudes of the residual strains of the wires. When the initial temperature is higher than A_s=34.5C, the composite plate can retain its initial configuration through a reverse transformation, as Figure (11) shows.

The phase transformations phenomena may be traced more adequately through studying the stress versus strain diagrams for various initial ambient temperatures. When the temperature is higher than A_s, the superelastic behavior is the dominant one whereas for temperatures below A_s, the shape memory and ferroelastic (in compressive stresses) behaviors may appear. In Figure (12), the stress-strain diagrams of the SMA wire are plotted for the central (impacted) point of the plate, for different initial temperatures.

As Figure (12) shows, both the martensite to austenite and austenite to martensite transformation stresses are higher for higher initial temperatures. The ferroelastic behavior may be noticed for temperatures that are less than A_s=34.5C. At the same time, the shape memory effects have led to residual strains (at the full unloading case) in these temperatures, as may be observed in Figure (12). The maximum residual strain belongs to the lowest temperature but slope of the stress-strain curve has decreased by decreasing the initial temperature. Due to using a kinematic hardening rule to model the ferroelastic behavior, the distances between the tensile and compressive transformation regions of each stress-strain curve are almost constant for temperatures that are below A_s. The hysteretic curves exhibit pure superelastic behaviors at temperature that are above A_s=34.5C, as Figure (12) shows. The largest hysteresis loop is associated with T_0=30C.

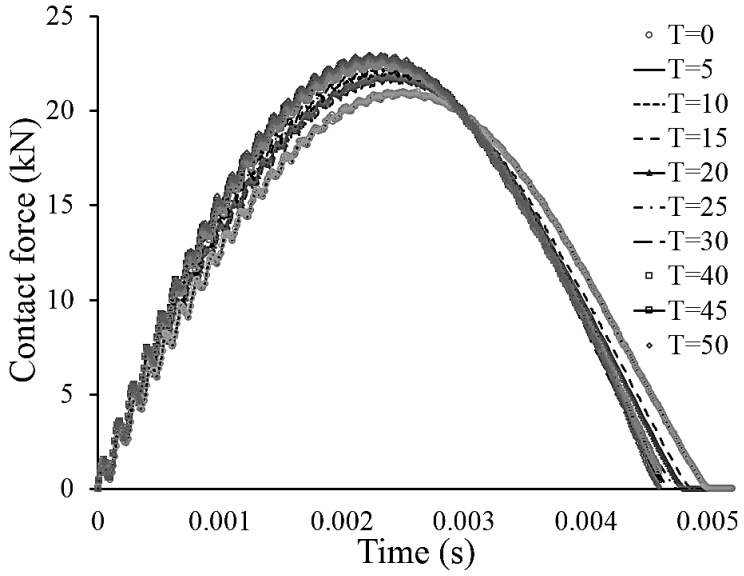

Figure 10 Time histories of the contact force of the plate with SMA wires, for various initial temperatures.

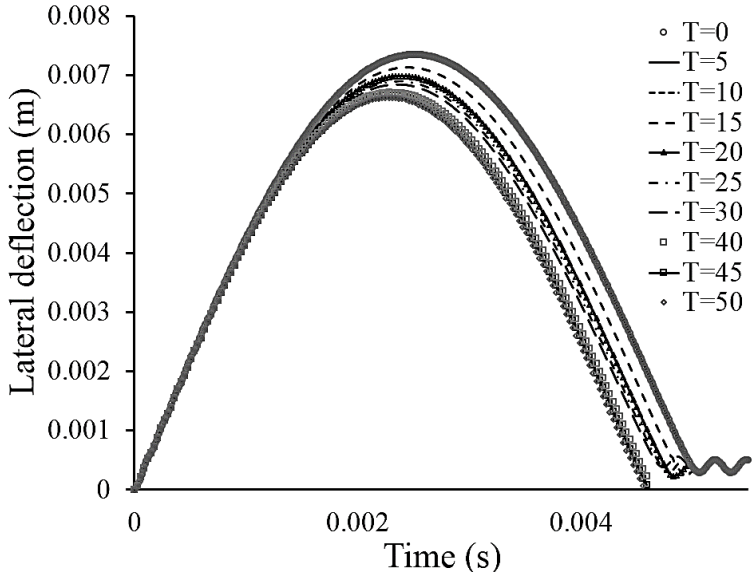

Figure 11 Time histories of the lateral deflection of the plate with SMA wires, for various initial temperatures.

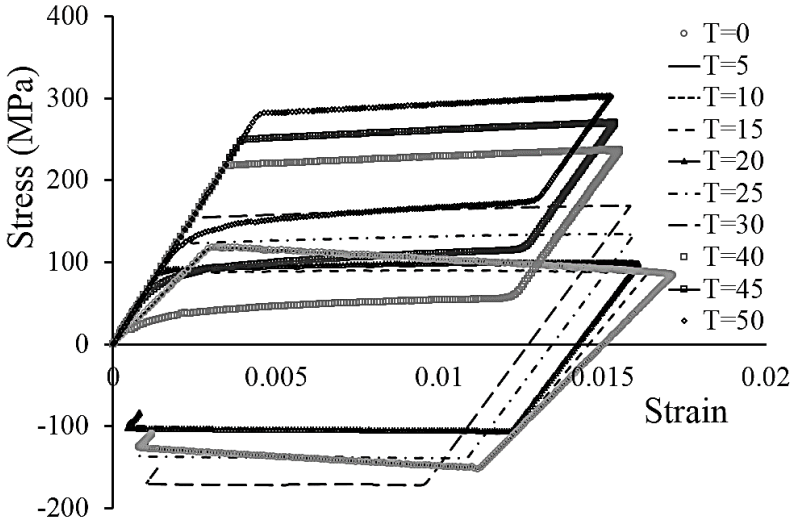

Figure 12 The stress-strain diagrams of the SMA wires at the central point of the plate, at various temperatures.

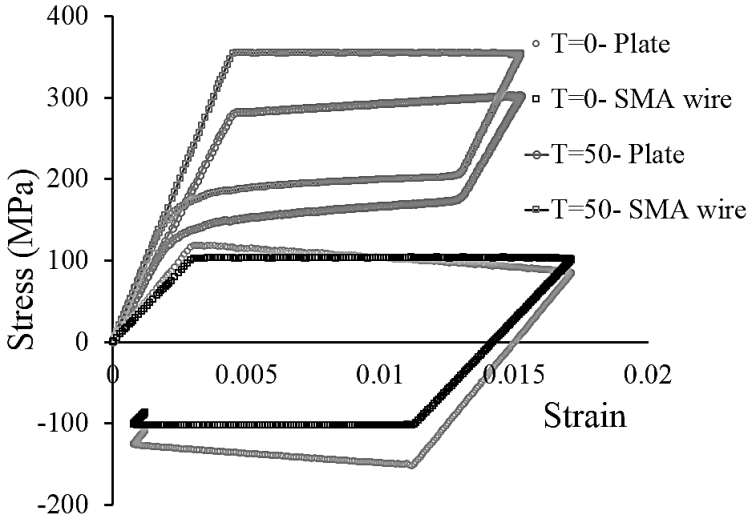

Figure 13 A comparison between the stresses induced in the lamina mixture and the SMA wire, at the central point of the plate.

Although a homogenization technique has been employed to derive the governing equations of the plate, the actual stress of the SMA wire that is different from that of the lamina mixture, has to be used to trace the transformation process. In this regard, a bridging tensor was introduced in Sec. 4.2 to describe the relations between these two distinct types of stresses. The stress-strain diagrams associated with the highest and lowest considered initial temperature, i.e., T_0=0 and 50C, are plotted in Figure (13) to demonstrate the differences between these two types of stresses. At T_0=0, the wires are initially in martensite phase. Therefore, the SMA stiffness is lower than that of the plate and it carries less stress than the plate material mixture whereas at T_0=50, the wire is initially in austenite phase whose stiffness is higher than that of the lamina and thus, the SMA wires bear higher stresses. These facts imply that in lower temperatures, the embedded SMA wires cannot increase the plate stiffness and the SMA wires have less efficiency in comparison to that of the higher temperatures. In other words, the SMA wire exhibits merely an elastic behavior in lower temperatures and the superelasticity behavior cannot be invoked.

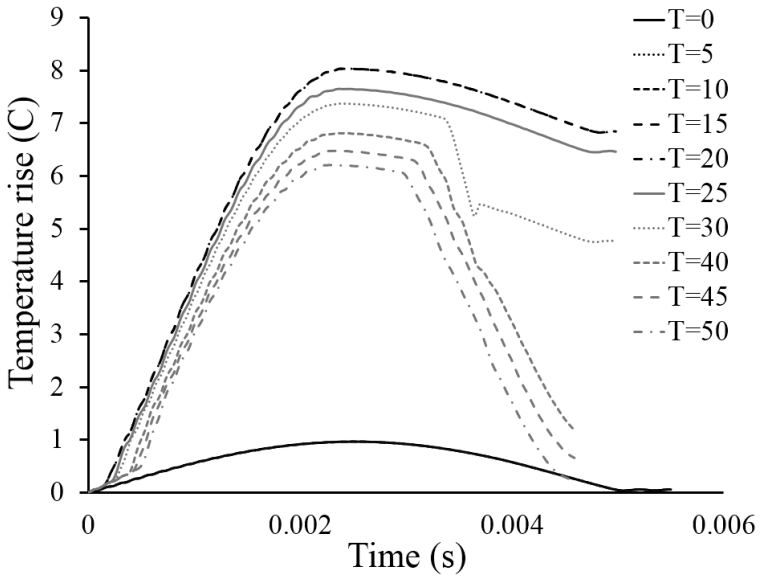

Figure 14 The resulting time variations of the temperature, for different initial temperatures.

As discussed in Sec. 2, the latent heat and transformation rate lead to heat generation in the SMA wires during the impact and consequently, lead to temperature rises in the wires. Although this phenomenon has not been captured properly by other researchers, it has been considered in the present research through using the coupled thermoelasticity theory and modifying Brinson's constitutive law.

Time variations of the martensite volume fraction are depicted in Figure (14) for various initial temperatures. Three kinds of behavior can be observed: (i) the initial martensite volume fraction is about 100% ($T_0<M_f$), (ii) the initial martensite volume fraction is about 0% but no reverse transformation to austenite phase occurs during unloading ($T_0<A_s$), (iii) forward and reverse transformation may take place ($T_0>A_s$).

Since the temperature variations stem from the martensite volume fraction rate, the first behavior leads to almost zero temperature variations. The second type of behavior, leads to the highest transformation rates and consequently, higher temperature rises in comparison to the third kind of behavior. These phenomena may be observed in Figure (15).

The smaller temperature rises belong to the smaller initial temperatures and are due to the coupling effects and not the transformation rate whereas the largest value are associated with the second type of behavior and include the combined coupling and transformation rate effects.

The temperature rise alters the shape of the SMA stress-strain diagram; it increases the transformation critical stress. Details of this effect on the stress-strain diagrams may be studied in Figure (16). This figure shows that the maximum stress is affected by the heat generation due to the transformation rate and the coupling. As may be deduced from Figure (16), ignoring the heat generation effects may lead to remarkable errors in the results.

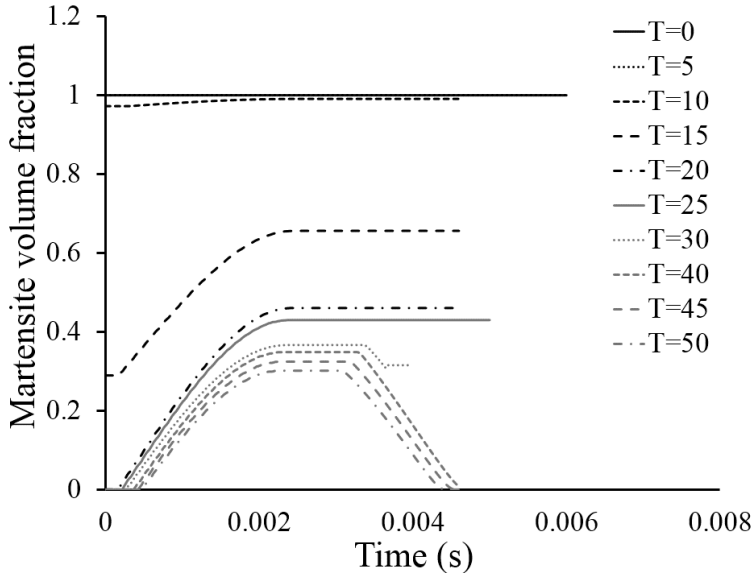

Figure 15 Time variations of the martensite volume fraction at different initial temperatures

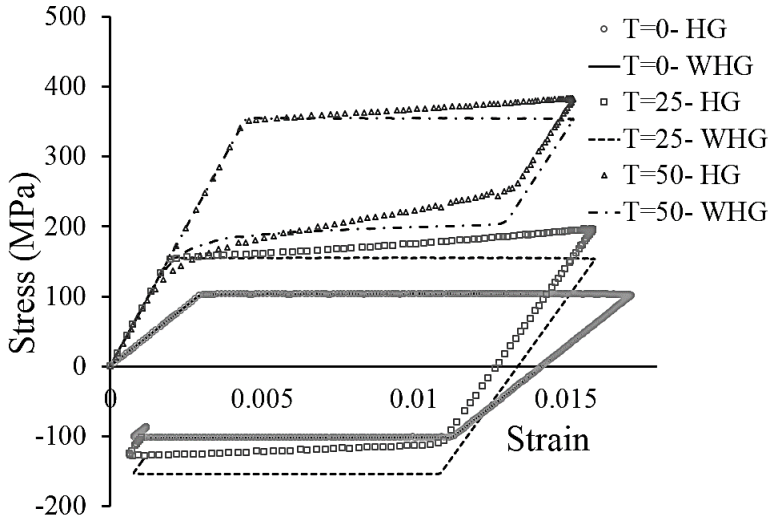

Figure 16 Effect of the temperature rise on the stress-strain diagrams. Results associated with heat generation and without heat generation assumptions are denoted by HG and WHG, respectively.

5 Conclusions

In the present paper, effects of the impact-induced heat generation and shape memory and ferroelastic behaviors of the SMA wires on impact responses and phase transformations of a hybrid SMA composite plate in thermal environments is investigated. To this end, a refined Helmholtz free energy function and refined constitutive and contact laws are proposed.

A return-map Newton-Raphson method is employed to expedite the numerical solution procedure. The written computer code is verified by the experimental results prepared by the authors. Comparative studies were presented to evaluate effects of the initial temperature, impact-induced temperature rise and shape memory and ferroelastic behaviors. Results confirm role of the SMA wires in increasing the impact strength of the composite plate within a special range of the initial temperatures. Lateral deflection of the composite plate decreases by increasing the initial temperature. Also, the heat generated due to the phase transformation affects the stress-strain diagrams.

References

[1] Lee, S.P., Lee, J.H., and Kang, K.W., "Residual Strength Distribution of Impacted Glass/Epoxy Laminates with Embedded Shape Memory Alloy at Low Temperature", Composite Structures, Vol. 93, pp. 324–330, (2011).

[2] Wu, Y., Wu, Y., Wang, Y., and Zhong, W., "Study on the Response to Low-velocity Impact of a Composite Plate Improved by Shape Memory Alloy", Acta Mechanica Solida Sin, Vol. 20, pp. 357–362, (2007).

[3] Shariyat, M., Moradi, M., and Samaee, S., "Enhanced Model for Nonlinear Dynamic Analysis of Rectangular Composite Plates with Embedded SMA Wires, Considering the Instantaneous Local Phase Changes", Composite Structures, Vol. 109, No. 1, pp. 106–118, (2014).

[4] Shariyat, M., and Moradi, M., "Enhanced Algorithm for Nonlinear Impact of Rectangular Composite Plates with SMA Wires, Accurately Tracing the Instantaneous and Local Phase Changes", Composite Structures, Vol. 108, No. 1, pp. 834–847, (2014).

[5] Shariyat, M., and Hosseini, S.H., "Accurate Eccentric Impact Analysis of the Preloaded SMA Composite Plates, Based on a Novel Mixed-order Hyperbolic Global–local Theory", Composite Structures, Vol. 124, pp. 140-151, (2015).

[6] Zurbitu, J., Santamarta, R., Picornell, C., Gan, W.M., Brokmeier, H.G., and Aurrekoetxea, J., "Impact Fatigue Behavior of Superelastic NiTi Shape Memory Alloy Wires", Materials Science and Engineering, Vol. 528, pp. 764–769, (2010).

[7] Helm, D., and Haupt, P., "Shape Memory Behavior: Modeling within Continuum Thermo-mechanics", International Journal of Solids and Structures, Vol. 40, pp. 827–849, (2003).

[8] Kadkhodaei, M., Rajapakse, R.K.N.D., Mahzoon, M., and Salimi, M., "Modeling of the Cyclic Thermo-mechanical Response of SMA Wires at Different Strain Rates", Smart Materials and Structures, Vol. 16, pp. 2091–2101, (2007).

[9] Monteiro, P.C.C., Savi, M.A., Netto, T.A., Manuel, P., and Pacheco, C.L., "A Phenomenological Description of the Thermo-mechanical Coupling and the Rate-dependent Behavior of Shape Memory Alloys", Journal of Intelligent Material Systems and Structures, Vol. 20, pp. 1675-1687, (2009).

[10] Morin, C., Moumni, Z., and Zaki, W., "A Constitutive Model for Shape Memory Alloys Accounting for Thermomechanical Coupling", International Journal of Plasticity, Vol. 27, pp. 748–767, (2011).

[11] Roh, J.H., "Thermomechanical Modeling of Shape Memory Alloys with Rate Dependency on the Pseudoelastic Behavior", Mathematical Problems in Engineering, Vol. 12, pp. 165-186, (2014).

[12] Shariyat, M., and Ghaznavi, A., "Simulation of the Superelastic and Shape Memory Effects Based on Various Micromechanical Models, under the Simple and Cyclic Mechanical and Thermal Loadings", Iranian J. Mech. Eng, Vol. 16, No. 1, pp. 78-103, (2014).

[13] Hetnarski, R.B., and Eslami, M.R., "*Thermal Stresses- Advanced Theory and Applications*", 1st Edition, Springer, Berlin, Germany, (2009).

[14] Eslami, M.R., Hetnarski, R.B., Ignaczak, J., Noda, N., Sumi, N., and Tanigawa, Y., "*Theory of Elasticity and Thermal Stresses*", Springer, Dordrecht, (2013).

[15] Brinson, L.C., and Lammering, R., "Finite Element Analysis of the Behavior of Shape Memory Alloys and their Applications", International Journal of Solids and Structures, Vol. 30, pp. 3261-3280, (1993).

[16] Turner, J.R., "Contact on a Transversely Isotropic Half-space, or between Two Transversely Isotropic Bodies", International Journal of Solids and Structures, Vol. 16, pp. 409–419, (1980).

[17] Yang, S.H, and Sun, C.T., "Indentation Law for Composite Laminates. In: Composite Materials: Testing and Design", 6th Conference, ASTM STP-787, pp. 425– 449, (1982).

[18] Eslami, M.R., "*Finite Elements Methods in Mechanics*", Springer, Switzerland, (2014).

[19] Brinson, L.C., "One Dimensional Constitutive Behavior Shape Memory Alloys: Thermo-mechanical Derivation with Non-constant Material Functions and Redefined Martensite Internal Variable", Journal of Intelligent Material Systems and Structures, Vol. 4, pp. 407-414, (1993).

[20] Songye, Z., and Yunfeng, Z., "A Thermo Mechanical Constitutive Model for Superelastic SMA Wire with Strain-rate Dependence", Smart Material Structure, Vol. 23, pp. 1696–1707, (2007).

[21] Huang, Z.M., "Simulation of the Mechanical Properties of Fibrous Composites by the Bridging Micromechanics Model", Composites: Part. A, Vol. 32, pp. 143–172, (2001).

[22] Jordan, E.M., and Ralph, C. S., "A Domain Wall Model for Hysteresis in Ferroelastic Materials", Journal of Intelligent Material Systems and Structures, Vol. 14, pp. 455-471, (2003).

Nomenclature

A_s	start temperatures of the austenite phase transformation
A_f	finishing temperatures of the austenite phase transformation
C_E	specific heat of material
C_{ijkl}	elasticity tensor
C_M	zero-stress slopes of the transformation regions into martensite
C_A	zero-stress slopes of the transformation regions into austenite phases
E_s	modulus of the SMA
E	Young's modulus
E_c	effective apparent modulus
E_A	Young's moduli of the austenite phases
E_M	Young's moduli of the martensite phases
f	Helmholtz free energy
F_{max}	maximum contact force
F_c	contact force
G	shear modulus
k_c	apparent contact stiffness
M_s	temperature of the start of the martensite transformation
$\mathcal{N}$	shape functions matrix
$\widehat{N}$	in-plane force quantities per unit length
q	eat flux vector
$\widehat{Q}_n$	transverse force quantities per unit length
Q_n	total transverse thermal heat flux
r	internal heat generation
S	entropy
T	temperature
T^*	critical temperature
T_0	initial temperature
U	nodal displacements of the reference plane
V	nodal displacements of the reference plane
V_s	SMA volume fraction of the hybrid composite
V_f	Volume fractions of the fiber
V_m	Volume fractions of the matrix
W	nodal displacements of the reference plane
w_i	vertical displacement of the indenter

Greek symbols

α	thermal expansion coefficient
α_{max}	maximum indentation
Λ	driving force
Δ	nodal displacement components vector
δ	displacement components vector
σ_{ij}	Cauchy's stress tensor
ε_{ij}	strain-rate tensor
$\bar{\varepsilon}_T$	thermal strains vector
ρ_0	mass density
ξ	martensite volume fraction
β_{ij}	stress-temperature coupling coefficient
ε_l	maximum recoverable strain
ξ_s	stress induced martensite volume fraction
Λ	latent heat of phase transformation
ν	Poisson's ratio
σ_s^{cr}	critical stresses associated with the start of the phase transformation process
σ_f^{cr}	critical stresses associated with the finish of the phase transformation process
Φ_x	nodal rotations of the cross-section in the x–z plane
Φ_y	nodal rotations of the cross-section in the y–z plane
ζ	natural coordinates of the element in the x- direction
η	natural coordinates of the element in the y-direction
Ω_0	area of the reference plane of the plate
Γ^σ	area of the reference the boundary of the plate

چکیده

در این تحقیق، پاسخ ضربه ورق کامپوزیتی مستطیلی شکل، تقویت شده با آلیاژ حافظه‌دار بررسی شده است. فرض شده است که ورق در یک محیط حرارتی قرار گرفته و بنابراین، بر خلاف پژوهشهای موجود، لازم است که اثرات حافظه‌داری و فروالاستیسیته را نیز علاوه بر اثر سوپرالاستیک مورد بررسی قرار داد.
معادلات حاکم بر مساله بر اساس تابع انرژی آزاد بهبود یافته پیشنهادی و معادلات ترموالاستیسیته ساختاری کوپل اصلاح شده استخراج شده و معادلات حاکم به شیوه المان محدود تحلیل شده است. برای این منظور از روش تکرار و الگوریتم ردیابی تغییر فاز مناسبی برای آلیاژهای حافظه‌دار استفاده شده است. نتایج این تحقیق نشان داده است که افزایش دمای ناشی از ضربه در آلیاژ حافظه‌دار، نرخ تغییرات حجم و دمای محیط به شدت بر روی فرایند تغییر فاز آلیاژ و نفوذ غیرخطی تاثیرگذار است.